Biosensors and Bioelectronics 66 (2015) 191–197

Contents lists available at ScienceDirect

Biosensors and Bioelectronics

journal homepage: www.elsevier.com/locate/bios

Green and facile synthesis of an Au nanoparticles@polyoxometalate/ordered mesoporous carbon tri-component nanocomposite and its electrochemical applications

Yufan Zhang, Xiangjie Bo*, Anaclet Nsabimana, Alexis Munyentwali, Ce Han, Mian Li, Liping Guo*

Faculty of Chemistry, Northeast Normal University, 130024 Changchun, PR China

ARTICLE INFO

Article history:
Received 1 September 2014
Received in revised form
30 October 2014
Accepted 14 November 2014
Available online 18 November 2014

Keywords:
Au@polyoxometalates
Ordered mesoporous carbon
Electrocatalysis
Acetaminophenol
H_2O_2
NADH

ABSTRACT

The one-pot synthesis of a well-defined Au nanoparticles@polyoxometalates/ordered mesoporous carbon (Au@POMs/OMC) tri-component nanocomposite is reported, which is facile, green and rapid. The polyoxometalates were used as both reductant and bridging molecules. The formation of these composite materials was verified by a comprehensive characterization using X-ray diffraction, X-ray photoelectron spectroscopy, energy-dispersive X-ray spectra, scanning electron microscopy, and transmission electron microscopy. The novel nanohybrids of Au@POMs/OMC can provide new features of electrocatalytic activities, because of the synergetic effects of Au nanoparticles and OMC materials. Most importantly, the amperometric measurements show that the Au@POMs/OMC nanohybrids have a high catalytic activity with a good sensitivity, long-term stability, wide linear range, low detection limit, and fast response towards acetaminophenol, H_2O_2, and NADH detection for application as an enzyme-free biosensor.

1. Introduction

Over the past decades, numerous research groups have consciously increased efforts to design and develop advanced materials with nanostructure. These materials have been studied widely as the electrode materials for the application of electrochemistry. Nanostructured carbon materials have been recognized as one of the most important electrode materials in the field of catalyst supports. Among these carbon-based materials, carbon nanotubes (Du et al., 2014; Kong and Chen, 2014; Saleh Ahammad et al., 2009; Scherbahn et al., 2014), graphene (Chaturvedi et al., 2014; Feng et al., 2014; Lu et al., 2014; Roy-Mayhew and Aksay, 2014), and carbon nanofibers (He et al., 2014; Huang et al., 2008; Ji et al., 2014a) are widely used as electrocatalyst supports. Besides these carbon materials, ordered mesoporous carbon (OMC) has been demonstrated to be a very attractive support material due to its unique properties, such as periodic mesoporous structure, large pore volume, good thermal as well as mechanical stability, exceptional chemical inertness, and excellent electrical conductivity (Park et al., 2013; Vu et al., 2013; Wu et al., 2013; Zhang et al., 2014b; Zhi et al., 2014). In particular, the large specific surface area of OMC may offer a platform for supporting other nanoentities to form novel hybrid nanostructures with synergetic effects. The combination of noble metal particles and OMC is of special interest; it is known to show an obviously enhanced electrocatalytic activity (Ahn et al., 2013; Kim et al., 2014; Wang et al., 2014; Zhang et al., 2011). However, the reduction processes of noble metal particles are complex and mostly needs high temperature and long time. Also the reaction process is normally not environmentally friendly.

Polyoxometalates (POMs) are well-defined early transition metal−−oxygen clusters with an enormous diversity of structures and properties. They are endowed with remarkable behaviors in several fields including catalysis, medicine and materials sciences (Babakhanian et al., 2014; Dolbecq et al., 2010; Fernandes et al., 2013; Hong et al., 2013; Nishimoto et al., 2014; Rhule et al., 1998; Stracke and Finke, 2014). POMs also are a class of photoactive materials used in homogeneous reactions or heterogeneous processes. In their reduced forms, their electron and proton transfer and/or storage abilities, may act as efficient donors or acceptors of several electrons without structural change (Biboum et al., 2010). Such reversible charge transfer ability makes POMs ideal candidates for electron exchange reactions. The reduced POMs have been shown to serve as reducing and capping agents for metal nanostructures. Moreover, POMs were reported to be adsorbed on

* Corresponding authors. Fax: +86 0431 85099762.
E-mail addresses: baoxj133@nenu.edu.cn (X. Bo), guolp078@nenu.edu.cn (L. Guo).

http://dx.doi.org/10.1016/j.bios.2014.11.022
0956-5663/

various solid materials and this property has recently been exploited for the stabilization of nanoparticles (Ji et al., 2014b; Li et al., 2011a, 2011b; Liu et al., 2011, 2012., 2013; Xing et al., 2013a, 2013b; Zhang et al., 2014a). Such active forms of POMs can be generated by a variety of techniques, including photochemistry, radiolysis, and electrochemistry.

Acetaminophen (AP) is generally is a major ingredient in numerous cold and influenza medications. It is also an effective and safe analgesic agent and is consequently used worldwide for the relief of mild to moderate pain associated with, e.g., headache, toothache, backache, arthritis, migraine, neuralgia, muscular aches, menstrual cramps, and postoperative pain (Wang et al., 2007). Hydrogen peroxide (H_2O_2), a well-known oxidizing agent, is not only a by-product of a large number of oxidase enzymes, but also an essential intermediate in biomedical, food production, pharmaceutical, industrial and environmental fields (Palanisamy et al., 2012). Nicotinamide adenine dinucleotide (NADH) is an important coenzyme involved in metabolic processes, widely existing in every cell of living organisms. It alternates between the reduced state NADH and the oxidized state NAD^+ for the production of ATP, and serves as hydrogen and electron carrier in cellular respiration and photosynthesis. The investigations of the redox reactivity of NADH and NAD^+ are important because a large number of dehydrogenase enzymes (>300) use these compounds as cofactors (Baskar et al., 2012; Teymourian et al., 2012). Therefore, the rapid and accurate detection of AP, H_2O_2, and NADH is of great significance.

Herein, we report an alternative, easy and green-chemistry type procedure for the decoration of Au nanoparticles on OMC using $H_3PW_{12}O_{40}$ (PW12, henceforth POMs for convenience) as the both reductant and bridging molecules. The as-prepared novel tri-component nanohybrids of Au@POMs/OMC extend the applications of support materials and provide new features of electrocatalytic activities. AP, H_2O_2, and NADH were selected as marking molecules to evaluate the electrochemical activity of the Au@POMs/OMC nanocomposite. The electrochemical results showed that the as-prepared electrode materials exhibited significant electrocatalytic activity towards AP, H_2O_2, and NADH in neutral solution, which proved that the as-synthesized Au@POMs/OMC could be used as electrochemical sensing platform for biomolecules.

2. Experimental

2.1. Chemical reagents

OMC was prepared using SBA-15 mesoporous silica as template by a nanohard-templating approach in our laboratory (Jun et al., 2000; Ryoo et al., 1999). POMs, isopropanol, and N,N′-dimethylformamide (DMF) (HPLC grade) were used as purchased from Beijing Chemical Co. Ltd. $HAuCl_4 \cdot 3H_2O$ was purchased from Sinopharm Chemical Reagent Co. Ltd. AP, H_2O_2, and β-NADH were obtained from Sigma. The 0.1 M phosphate buffer solution (PBS pH 7.0), which was made up from NaH_2PO_4, Na_2HPO_4, and H_3PO_4, was employed as a supporting electrolyte. All other reagents were of analytical grade, and all solutions were prepared using double distilled water.

2.2. Instrumentation

All the electrochemical experiments were performed with a CHI 830B electrochemical Analyzer (CH Instruments, Shanghai Chenhua Instrument Corporation, China). Electrochemical impedance spectroscopy (EIS) was conducted using a PARSTAT 2273 Potentiostats-Electrochemistry Workstation (AMETEK Instruments, USA) in a 0.1 M KCl solution containing 5.0 mM $K_3Fe(CN)_6/K_4Fe(CN)_6$, from 0.1 Hz to 10.0 kHz. X-Ray diffraction (XRD) patterns were obtained on an X-rayD/max-2200vpc (Rigaku Corporation, Japan) instrument operated at 40 kV and 20 mA using Cu Kα radiation ($k=0.15406$ nm). Scanning electron microscopy (SEM) image was determined with a PhilipsXL-30 ESEM, operating at 3.0 kV. Transmission electron microscopy (TEM) images and energy-dispersive X-ray spectra (EDX) were obtained using a JEM-2100F transmission electron microscope JEOL (Japan) operating at 200 kV. X-ray photoelectron spectroscopy (XPS) measurements were performed with a thermo ESCA LAB spectrometer (USA). A conventional three electrode cell was used; the working electrode was glassy carbon electrode (GCE) or the modified electrode; a platinum electrode was used as the counter electrode whereas an Ag/AgCl (in saturated KCl solution) electrode served as a reference electrode. All potentials in this paper were measured and reported versus Ag/AgCl. It is worth mentioning that in this study, all the sample solutions were purged with purified nitrogen for 20 min to remove oxygen prior to the beginning of a series of experiments and all experiments were carried out at laboratory temperature.

2.3. Preparation of the modified electrodes

Prior to the modification, GCE (model CHI104, 3 mm diameter) was polished before each experiment with 1, 0.3 and 0.05 μm alumina power, rinsed thoroughly with double distilled water between each polishing step, and then sonicated successively in 1:1 nitric acid, absolute alcohol, double distilled water. The cleaned electrode was dried with nitrogen stream for the next modification. To prepare the modified electrodes, 5 mg of the electrode materials were dispersed into 1 mL DMF to give homogeneous suspension upon bath sonication. 5 μL of the suspension was dropped onto GCE and the electrode was then dried at room temperature.

2.4. Synthesis of tri-component nanohybrids of Au@POMs/OMC-x

The POMs were firstly reduced photochemically. A 500 W Hg lamp was used as a ultra-violet (UV) light source. In a typical synthesis, POMs (100 mL, 1 mM) were added to a quartz bottle and mixed with isopropanol (700 μL). Then, the resulting solution was irradiated under the UV light for 30 min with stirring. The concentration of the reduced POMs was controlled by varying the irradiation time. This solution of reduced POMs was mixed with prepared OMC suspension (10 mL, 2 mg mL^{-1}) and aqueous solution of $HAuCl_4 \cdot 3H_2O$ (1 mL) at room temperature, and then stirred for 10 min; the tri-component nanohybrids were prepared. The suspension was isolated by centrifugation at 8000 rpm, followed by consecutive washing/centrifugation cycles several times with doubly distilled water. The obtained Au@POMs/OMC-*x* was dried in a vacuum oven at 60 °C for 36 h. For optimization of the nanocomposite, different concentrations of $HAuCl_4 \cdot 3H_2O$ (2.5 mM, 50 mM, and 1 M) were selected to be added to the mixture. The Au@POMs/OMC-*x* materials are referred to as Au@POMs/OMC-1, Au@POMs/OMC-2, and Au@POMs/OMC-3, where 1, 2, and 3 represent the different concentrations of $HAuCl_4 \cdot 3H_2O$ (2.5 mM, 50 mM, and 1 M) in the synthesis procedure, respectively.

For comparison, the nanocomposites without Au nanoparticles decoration (POMs/OMC) are also prepared. In a typical synthesis, OMCs suspension (10 mL, 2 mg mL^{-1}) were added in the initial POMs (100 mL, 1 mM) by ultrasonication for 20 min, followed by filtering, washing several times and drying in a vacuum oven at 60 °C for 36 h.

3. Results and discussion

3.1. Characterization of the as-prepared samples

The preparation of Au@POMs/OMC-*x* is presented in Scheme 1. During the synthesis, the POMs not only serve as reducing agents for Au^{3+}, but also as bridging molecules for Au nanoparticles and OMC (Li et al., 2011a, 2011b). The morphologies of OMC and Au@POMs/OMC-*x* were initially characterized by SEM and TEM. Fig. 1A shows SEM image of the pure OMC. The OMC was made of small grains, which have a submicrometer-scale particle size with the length of 0.5–1.5 μm. Fig. 1B shows TEM image of the OMC before decoration with Au@POMs. Bright contrast strips on the planar TEM image represent the pore-wall images, whereas dark contrast cores display empty channels. The typical large-scaled TEM images of Au@POMs/OMC-2 are presented in Fig. 1C and Fig. S1. Moreover, for low-scaled image of Au@POMs/OMC-2 sample, in Fig. 1D, it is shown that Au nanoparticles are uniformly dispersed on the surface of OMC. The average diameter of these Au nanoparticles determined from a statistical study of 100 nanoparticles is 4.5 nm (Fig. 1E). The high-resolution (HRTEM) image of Au@POMs/OMC-2 shown in Fig. 1F reveals that the spacing of the adjacent fringes along the wire growth direction is 0.23 nm, corresponding to the {111} interplanar distance of face-centered cubic structure. The typical TEM image of Au@POMs/OMC-1 is shown in Fig. S2, it shows that a small amount of Au nanoparticles are dispersed on the surface of OMC. However, for Au@POMs/OMC-3, the agglomerates of Au nanoparticles look totally different (Fig. S3). The image clearly illustrates that too much Au nanoparticles can form Au cluster, and cannot be uniformly dispersed on the surface of OMC.

The composition of as-synthesized Au@POMs/OMC-2 was confirmed by EDX spectroscopy, as shown in Fig. 2A. It shows the peaks corresponding to carbon, oxygen, Au, and tungsten elements (the strong peaks of Cu are from the copper grid), therefore confirming the existence of Au@POMs in the Au@POMs/OMC nanohybrids. The XRD patterns of the Au@POMs/OMC-2 are presented in Fig. 2B. The observed characteristic peaks at 38.4° and 44.3° are assigned to the (111) and (200) planes of Au crystals of face-centered cubic structure. Moreover, diffraction peaks from the POMs were also observed. Their presence constitutes an unquestionable evidence for the formation of tri-component nanohybrids of Au@POMs/OMC-2. In addition, XRD patterns of Au@POMs/OMC-1 and 3 are presented in Fig. S4. The content of the obtained materials were further determined using XPS analysis. The XPS wide scan spectra of as-prepared Au@POMs/OMC-1, 2, and 3 nanocomposites are depicted in Fig. S5. The elemental composition of different materials obtained from XPS analysis is shown in Table S1. The XPS spectrum of the as-prepared nanohybrids of Au@POMs/OMC-2 shows the Au*4f* 7/2 and *4f* 5/2 doublet with the binding energies of 84.0 and 87.7 eV, respectively (Fig. 2C). These values unambiguously suggest that Au nanoparticles are present only in the metallic form, indicating the formation of Au nanoparticles on the surface of OMCs. The presence of W was also detected by XPS despite the thorough washing of the samples. As shown in Fig. 2D, there is W*4f* 5/2 and *4f* 7/2 doublet with the binding energies of 36.13 and 38.23 eV respectively. These values indicate that W is in its full oxidation form in POMs when assembling in the nanohybrids. In addition, the Au*4f* and W*4f* doublets of both Au@POMs/OMC-1 and 3 are presented in Fig. S6. From the characterization results of EDX, XRD, and XPS, it is clearly shown that, except for strong peaks of Au, tungsten is present in the samples, confirming the POMs existence around Au NPs. This happens because the reduced POMs were serving as reducing agents for Au^{3+}, and then the POMs with oxidation form were wrapped on the surface of Au nanoparticles. This is not surprising because it is in perfect agreement with the existing literature (Wang et al., 2009; Zhang et al., 2009).

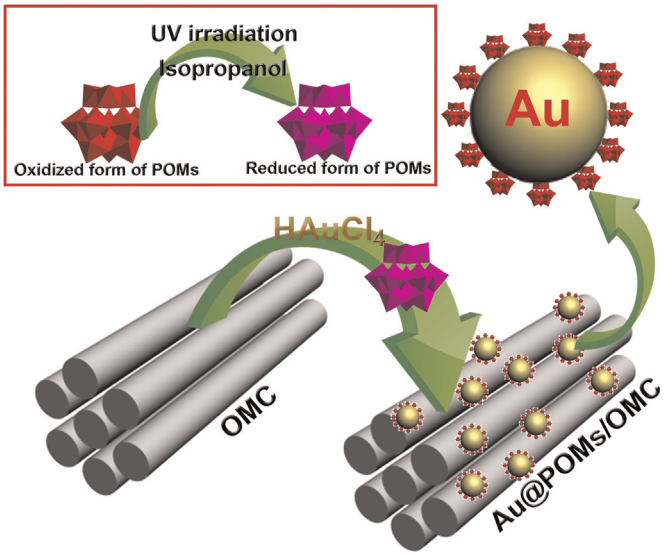

Scheme 1. Illustration of the preparation of Au@POMs/OMC tri-component nanohybrids.

EIS experiments were conducted to analyze the capability of electron transfer of different electrode materials. Fig. S7 shows the Nyquist plots of the EIS for the bare GCE, OMC–GCE, and Au@POMs/OMC-1, 2, and 3-GCE. The charge transfer resistance (R_{ct}) values for the $Fe[(CN)_6]^{4-/3-}$ couple at different electrodes were recorded and are shown in Table S2. It demonstrates that OMC can form a fast electron pathway between the electrode and the electrolyte and can therefore serve as a good platform for sensing applications. However, it is worth mentioning that the amount of Au nanoparticles and its quality of dispersion are the key factors to the rate of electron transfer. At the Au@POMs/OMC-1-GCE, the amount of Au is relatively low, so that the electron transfer rate cannot achieve the best results. As far as Au@POMs/OMC-3-GCE is concerned, the too big amount of Au nanoparticles not only raises the costs of production, it may also cause the nanoparticles to agglomerate, and this makes it ineffective to the electron transfer. Compared with the two nanohybrids, Au@POMs/OMC-2 possesses reasonable coverage amount and well dispersion of Au nanoparticles on the OMC, which can facilitate the rate of electron transfer. This is the reason why it has the best electrocatalytic ability among the Au@POMs/OMC samples investigated in this study, as shown in the following section.

3.2. Electrocatalysis of AP, H_2O_2, and NADH and their detection

The electrocatalytic properties of the different electrodes towards AP detection were investigated. Fig. 3A displays the CVs behaviors of the bare GCE, OMC–GCE, and Au@POMs/OMC-2-GCE in 0.1 M PBS (pH = 7.0) solution in the presence of 1.0 mM AP over a potential range of 0–0.8 V at a scan rate of 50 mV s^{-1}. Clearly, there is a small electrochemical response at bare GCE. However, a significantly enhanced electrochemical response towards AP oxidation is obtained after modification by the OMC. Au@POMs/OMC-2-GCE shows an obvious decrease in overpotential as well as response current increase for AP oxidation compared with bare GCE and OMC–GCE. The CVs of the Au@POMs/OMC-1 and 3-GCE for AP oxidation are presented in Fig. S8. It is shown that, among the synthesized Au@POMs/OMC electrode materials, Au@POMs/OMC-2 sample possesses the best electrocatalytic activity towards AP oxidation (Table S3). The results indicate that the presence of Au@POMs/OMC-2 made the electron transfer much easier

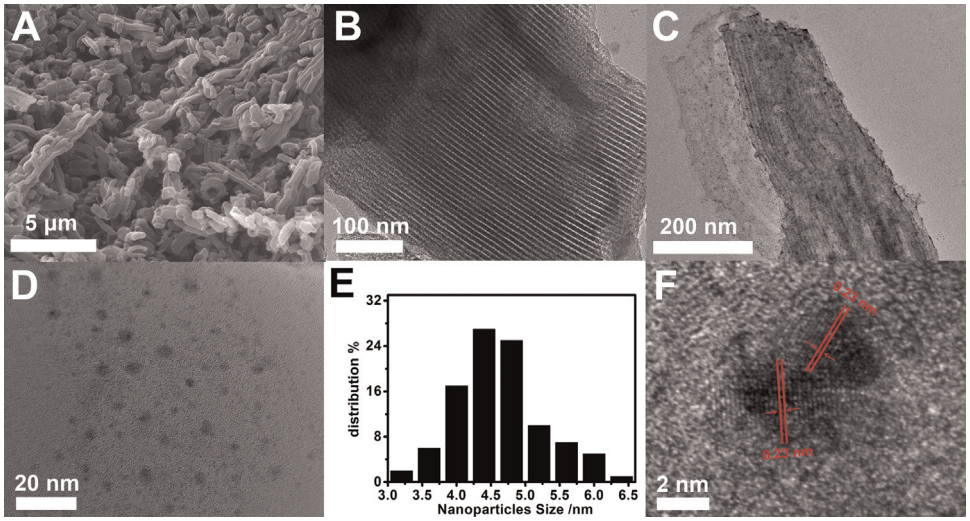

Fig. 1. (A) SEM image of OMC, (B) TEM image of OMC, (C) and (D) TEM images of Au@POMs/OMC-2, (E) columnar distribution of Au nanoparticles size for Au@POMs/OMC-2, and (F) HRTEM image of Au@POMs/OMC-2.

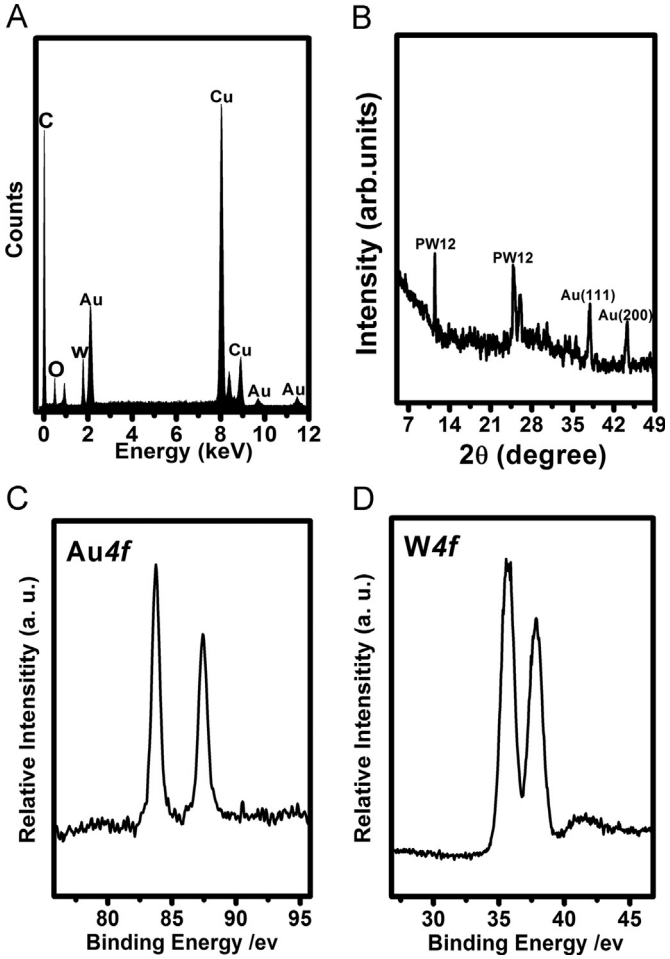

Fig. 2. (A) EDX spectra of Au@POMs/OMC-2. (B) XRD patterns of the Au@POMs/OMC-2. (C and D) High-resolution XPS spectra of Au*4f* and W*4f* spectra of Au@POMs/OMC-2 nanohybrids.

compared with that of other Au@POMs/OMC-*x* samples. Thus, we focused on the investigation of the AP at the Au@POMs/OMC-2-GCE. Fig. 3B shows a typical amperometric current–time curve of Au@POMs/OMC-2-GCE with successive additions of AP (pH 7.0). The best potential chosen to be applied, based on the CVs measurements, was +0.33 V. Inset a of Fig. 3B shows the amperometric response of low concentration of AP at Au@POMs/OMC-2-GCE. This figure shows that Au@POMs/OMC-2-GCE responds very rapidly to the changes in the level of AP, producing steady-state signals in less than 2 s (inset b of Fig. 3B). The relationship between AP concentration and current signal for Au@POMs/OMC-2-GCE is illustrated in Fig. 3C. Error bars are the standard deviations of five repetitive experiments (RSD=4.9%). The current increased linearly with the good linear ranges from 1 to 57 μM (R^2=0.997, n=15) having a sensitivity of 29.75 μA μM^{-1} and from 57 to 3000 μM (R^2=0.995, n=12) with a sensitivity of 33.18 μA μM^{-1}. The detection limit was calculated to be 0.29 μM. The performance of the Au@POMs/OMC-2-GCE was also compared with other AP sensors (Table S4).

To evaluate the selectivity of the Au@POMs/OMC-2-GCE in the detection of AP, we investigated the influence of several possible interferences in the electrochemical experiments (Fig. S9). For AP, an ignorable interference was observed for the fructose, sucrose, citric acid, and tryptophan. Some interference, such as uric acid and NADH was also obtained. In order to evaluate the practical application of the fabricated electrode, it was used to detect the concentration of AP from paracetamol tablets under the optimum laboratory conditions. To demonstrate the performance of the proposed method in a real sample analysis, the concentration of AP in paracetamol tablet was analyzed using i-t method based on the Au@POMs/OMC-2-GCE by the standard addition method. It was found that the content of AP in paracetamol tablet was 623 mg/g per tablet (n=5), RSD is 3.2%. The result is similar with that of the standard concentration of paracetamol tablet (600 mg/g). This means that the proposed i-t method using Au@POMs/OMC-2-GCE is applicable for the fast and accurate determination of AP in pharmaceutical formulations.

In Fig. 4A, the CVs for H_2O_2 reduction at different electrodes were compared. It shows a weak electrocatalytic reduction current towards H_2O_2 at bare GCE. For OMC–GCE, the reduction results exhibit a marked increase in current for H_2O_2 reduction compared with GCE. More interestingly, the catalytic activity of Au@POMs/OMC-2-GCE is evident from a decrease in overpotential as well as response current increase for H_2O_2 reduction compared with bare GCE and OMC–GCE. Moreover, compared with Au@POMs/OMC-1 and -3-GCE (Fig. S10), the Au@POMs/OMC-2-GCE shows the best catalytic activity for H_2O_2 reduction. Thus, we focused on the investigation of the electrochemical properties of Au@POMs/OMC-2. Fig. 4B displays the current–time responses of Au@POMs/OMC-2

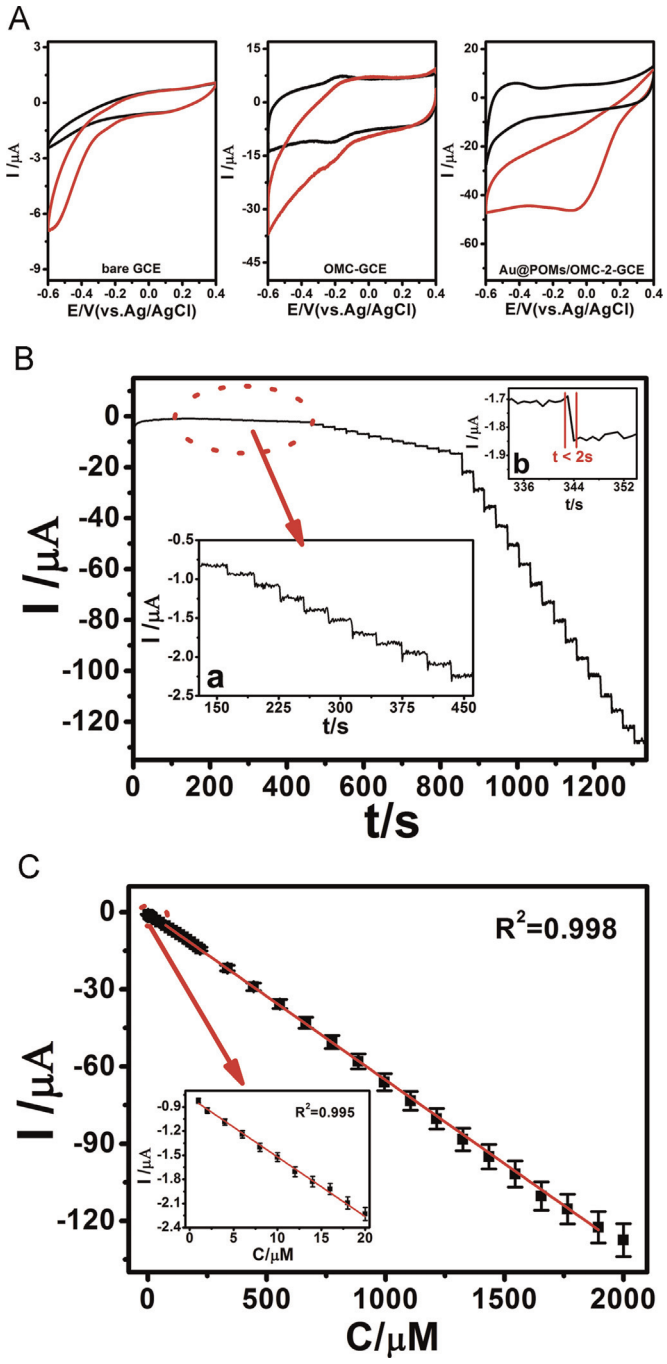

Fig. 3. (A) CVs of bare GCE, OMC–GCE, and Au@POMs/OMC-2-GCE in the presence of 1.0 mM AP (pH=7.0). Scan rate: 50 mV s^{-1}. (B) Typical amperometric current–time curve of Au@POMs/OMC-2-GCE with successive additions of AP (pH=7.0). Inset a: The amperometric response with successive addition of AP at lower concentration. Inset b: The current response time after the AP addition at Au@POMs/OMC-2-GCE. (C) The linear dependence of the current signal on AP concentration for Au@POMs/OMC-2-GCE. Inset: the amperometric response with successive addition of AP at lower concentration.

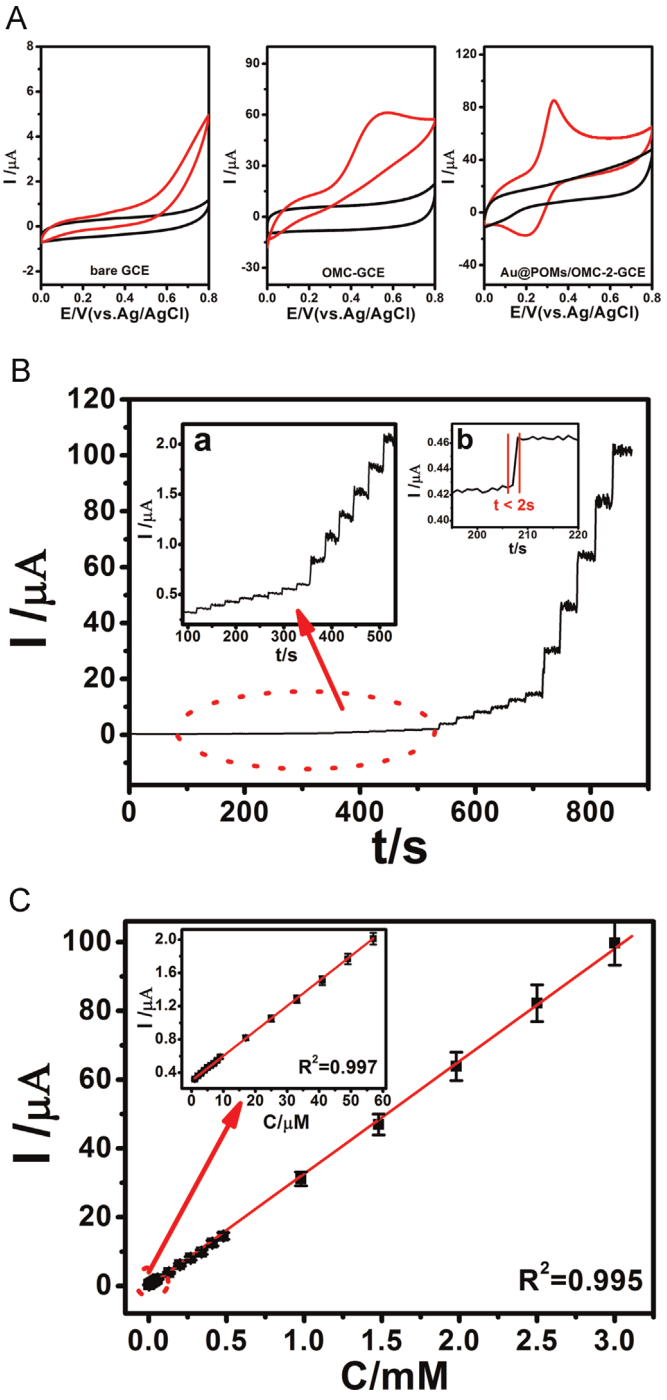

Fig. 4. (A) CVs of bare GCE, OMC–GCE, and Au@POMs/OMC-2-GCE in the presence of 1.0 mM H_2O_2 (pH=7.0). Scan rate: 50 mV s^{-1}. (B) Typical amperometric current–time curve of Au@POMs/OMC-2-GCE with successive additions of H_2O_2 (pH=7.0). Inset a: The amperometric response with successive addition of H_2O_2 at lower concentration. Inset b: The current response time after the H_2O_2 addition at Au@POMs/OMC-2-GCE. (C) The linear dependence of current signal on H_2O_2 concentration for Au@POMs/OMC-2-GCE. Inset: the amperometric response with successive addition of H_2O_2 at lower concentration.

for H_2O_2 detection at pH=7.0 with the applied potential of −0.03 V. Inset a of Fig. 4B shows the amperometric response of low concentration of H_2O_2 at Au@POMs/OMC-2. The current response of Au@POMs/OMC-2 generally reached a steady-state level within 2 s after the H_2O_2 addition (inset b of Fig. 4B). The corresponding calibration plot for the reduction of H_2O_2 at Au@POMs/OMC-2 is shown in Fig. 4C. The H_2O_2 sensor displays a linear range of 1–20 μM (R^2=0.995, n=11) with a sensitivity of 72.44 μA mM^{-1} and 20–1900 μM (R^2=0.998, n=29) with a sensitivity of 55.72 μA mM^{-1}. The detection limit was calculated to be 0.36 μM with the signal to noise ratio of three (S/N=3). The reproducibility of the sensor was also investigated by current–time method for five repetitive measurements with additions of 100 μM H_2O_2 at −0.03 V (pH=7.0). The RSD of the sensitivity was less than 3.0%. When the Au@POMs/OMC-2 was stored at 4 °C for two weeks, the current response to 100 μM H_2O_2 remained 94.5% of its original value, suggesting the long-term stability of the modified electrode.

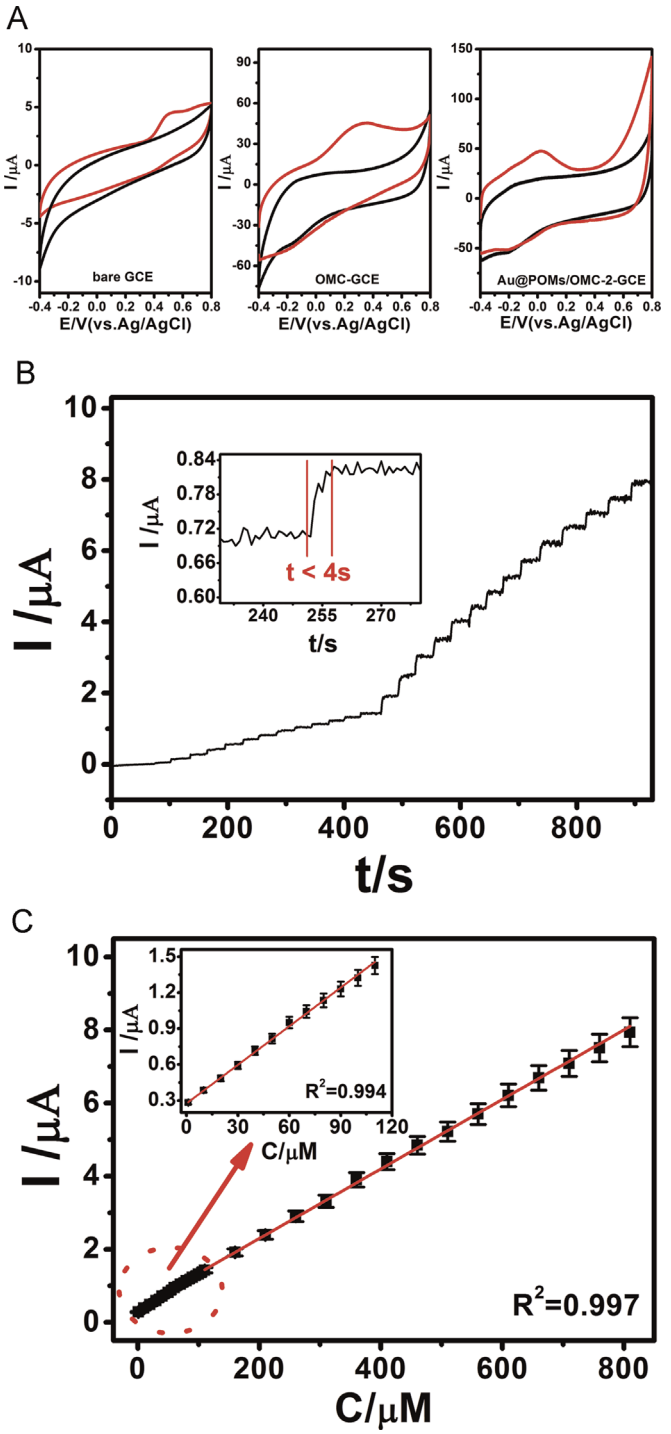

Fig. 5. (A) CVs of bare GCE, OMC–GCE, and Au@POMs/OMC-2-GCE in the presence of 0.5 mM NADH (pH=7.0). Scan rate: 50 mV s^{-1}. (B) Typical amperometric current–time curve of Au@POMs/OMC-2-GCE with successive additions of NADH (pH=7.0). Inset: The current response time after the NADH addition at Au@POMs/OMC-2-GCE. (C) The linear dependence of current signal on NADH concentration for Au@POMs/OMC-2-GCE.

The performance of the Au@POMs/OMC-2 was also compared with other H_2O_2 sensors (Table S5).

Possible interferences for the detection of nitrobenzene at the Au@POMs/OMC-2-GCE were also investigated by addition of various pollutants in the presence of 200 μM H_2O_2 (Fig. S11). From the results, hydrazine, nitrobenzene, aniline, 2-toluidine, toluene, and phenol and have no obvious influence on the H_2O_2 detection at Au@POMs/OMC-2-GCE with their concentrations of 10-fold higher than that of H_2O_2. H_2O_2 in commercially disinfectant solution was detected by the as-prepared Au@POMs/OMC-2-GCE. Briefly, 100 μL commercially disinfectant samples were added into 10 mL PBS solution, and then the current response was recorded at −0.03 V. The results are satisfying and agree with the results obtained by Au@POMs/OMC-2-GCE sensor in standard concentration (standard concentration of the commercially disinfectant is 3%). These illustrate our electrode could be used for detecting not only the standard H_2O_2, but also the real samples accompanying good reliability.

Fig. 5A displays the CVs of different electrodes in the presence of NADH. There is a small electrochemical response at bare GCE. However, it exhibits obvious decrease in overpotential with increase in peak current for NADH oxidation at OMC–GCE compared with bare GCE. Additionally, the oxidation current of NADH at the Au@POMs/OMC-2 exhibits an increased signal, which is 19.1- and 1.6-fold higher than that of the bare GCE and OMC–GCE, respectively. The catalytic activities of Au@POMs/OMC-1 and 3-GCE for NADH oxidation are shown in Fig. S12. The values of overpotential and peak current of Au@POMs/OMC-*x*-GCE for NADH oxidation are presented in Table S3. Thus, Au@POMs/OMC-2 was selected as an amperometric sensor for NADH detection. In this study, the current–time method was employed to detect NADH at Au@POMs/OMC-2-GCE (Fig. 5B). It is very clear that the current response of Au@POMs/OMC-2 generally reached a steady-state level within 4 s after the NADH addition (inset of Fig. 5B). The calibration curve of oxidation current is depicted in Fig. 5C, it exhibits steady amperometric response towards NADH in the linear concentration range of 1–110 μM (R^2=0.994, n=12) with a sensitivity of 10.54 μA mM^{-1} and from 110 to 810 μM (R^2=0.997, n=15) with a sensitivity of 9.35 μA mM^{-1}. The detection limit is 0.41 μM. The reproducibility of the sensor was also investigated by current–time method. The RSD of current signal for 200 μM NADH was less than 5.2% for five measurements, for the same electrode. After being stored at 4 °C for two weeks, 9.4% current loss was observed at Au@POMs/OMC-2 on the amperometric response of 200 μM NADH. The detailed comparison of NADH detection performance using different NADH sensors is summarized in Table S6. Possible interferences for the detection of nitrobenzene at the Au@POMs/OMC-2-GCE were also investigated by addition of various pollutants in the presence of 0.1 mM NADH (Fig. S13). The interference of compounds, namely fructose, sucrose, citric acid, tryptophan, uric acid, and AP were tested under the optimized experimental conditions. It was also found that these compounds have no response when their concentrations were 10-fold higher than NADH except uric acid and AP.

In addition, the POMs/OMC nanocomposites as the electrocatalyst for AP, H_2O_2, and NADH are also recorded. The CVs for AP, H_2O_2, and NADH at POMs/OMC–GCE were presented (Fig. S14). It shows that the response current and overpotential for AP (Fig. S14A), H_2O_2 (Fig. S14B), and NADH (Fig. S14C) at POMs/OMC–GCE are consistent with that of the OMC–GCE. Interestingly, the catalytic activity of Au@POMs/OMC-*x*-GCE is evident from a decrease in overpotential as well as response current increase for these biomoleculars compared with POMs/OMC–GCE and OMC–GCE. The results indicate that Au nanoparticles play an important role in the Au@POMs/OMC-*x*-GCE tri-component nanohybrids.

By and large, from these findings of electrochemical experiments, the Au@POMs/OMC-2 tri-component nanohybrids displayed the best electrocatalytic activity among the as-synthesized samples investigated in this study. The reason is attributed to the well dispersion of Au nanoparticles on the OMC and the suitable configurations of Au nanoparticles in the Au@POMs/OMC-2 nanohybrids. They are the key factors in determining the heterogeneous electron transfer rate of electrode. Therefore, the Au@POMs/OMC-2 sample could offer a favorite microenvironment for

transferring species in solution, and would also be beneficial for accelerating electron transfer between the electrode and species in solution.

4. Conclusions

Au@POMs/OMC tri-component nanohybrids have successfully been prepared for the first time using a facile, green, and one-pot synthesis method. The POMs were used as both the reductant and bridging molecules. The OMC can offer a platform for supporting Au@POMs to form novel hybrid nanostructures with synergetic effects. The amounts of Au were selected in a reasonable optimization. These as-prepared samples were verified by detailed characterization analyses and electrochemical investigation. Au@POMs/OMC-2 tri-component nanohybrids presented the best electrocatalytic activity among the as-synthesized samples. A sensitive biosensor for AP, H_2O_2, and NADH was developed based on the Au@POMs/OMC-2-GCE, which showed wide linear range, low detection limit, high sensitivity, and good stability. In point of fact, the successful fabrication of Au@POMs/OMC holds great promise for the design of biosensors, and is a promising way to promote the development of new electrode materials.

Acknowledgments

The authors gratefully acknowledge the Fundamental Research Funds for the Central Universities (Nos. 14ZZ2225 and 14QNJJ011) and the China Postdoctoral Science Foundation funded Project (2014M550164).

Appendix A. Supplementary material

Supplementary data associated with this article can be found in the online version at 10.1016/j.bios.2014.11.022

References

Ahn, C.Y., Cheon, J.Y., Joo, S.H., Kim, J., 2013. J. Power Sour. 222, 477–482.
Babakhanian, A., Kaki, S., Ahmadi, M., Ehzari, H., Pashabadi, A., 2014. Biosens. Bioelectron. 60 (0), 185–190.
Baskar, S., Chang, J.L., Zen, J.M., 2012. Biosens. Bioelectron. 33 (1), 95–99.
Biboum, R.N., Keita, B., Franger, S., Njiki, C.P.N., Zhang, G., Zhang, J., Liu, T., Mbomekalle, I.M., Nadjo, L., 2010. Materials 3 (1), 741–754.
Chaturvedi, P., Vanegas, D.C., Taguchi, M., Burrs, S.L., Sharma, P., McLamore, E.S., 2014. Biosens. Bioelectron. 58 (0), 179–185.
Dolbecq, A., Dumas, E., Mayer, C.R., Mialane, P., 2010. Chem. Rev. 110 (10), 6009–6048.
Du, X., Miao, Z., Zhang, D., Fang, Y., Ma, M., Chen, Q., 2014. Biosens. Bioelectron. 62 (0), 73–78.
Feng, L., Zhang, Z., Ren, J., Qu, X., 2014. Biosens. Bioelectron. 62 (0), 52–58.
Fernandes, D.M., Barbosa, A.D.S., Pires, J., Balula, S.S., Cunha-Silva, L., Freire, C., 2013. ACS Appl. Mater. Interfaces 5 (24), 13382–13390.
He, F., Hu, Z., Liu, K., Zhang, S., Liu, H., Sang, S., 2014. J. Power Sour. 267 (0), 188–196.
Hong, L., Gui, Y., Lu, J., Hu, J., Yuan, J., Niu, L., 2013. Int. J. Hydrog. Energy 38 (25), 11074–11079.
Huang, J., Liu, Y., Hou, H., You, T., 2008. Biosens. Bioelectron. 24 (4), 632–637.
Ji, L., Gu, M., Shao, Y., Li, X., Engelhard, M.H., Arey, B.W., Wang, W., Nie, Z., Xiao, J., Wang, C., Zhang, J.-G., Liu, J., 2014a. Adv. Mater. 26 (18), 2901–2908.
Ji, Y., Shen, L., Wang, A., Wu, M., Tang, Y., Chen, Y., Lu, T., 2014b. J. Power Sour. 260 (0), 82–88.
Jun, S., Joo, S.H., Ryoo, R., Kruk, M., Jaroniec, M., Liu, Z., Ohsuna, T., Terasaki, O., 2000. J. Am. Chem. Soc. 122 (43), 10712–10713.
Kim, N.-I., Cheon, J.Y., Kim, J.H., Seong, J., Park, J.-Y., Joo, S.H., Kwon, K., 2014. Carbon 72 (0), 354–364.
Kong, L., Chen, W., 2014. Adv. Mater. 26 (7), 1025–1043.
Li, S., Yu, X., Zhang, G., Ma, Y., Yao, J., de Oliveira, P., 2011a. Carbon 49 (6), 1906–1911.
Li, S., Yu, X., Zhang, G., Ma, Y., Yao, J., Keita, B., Louis, N., Zhao, H., 2011b. J. Mater. Chem. 21 (7), 2282–2287.
Liu, R., Li, S., Yu, X., Zhang, G., Ma, Y., Yao, J., 2011. J. Mater. Chem. 21 (38), 14917–14924.
Liu, R., Li, S., Yu, X., Zhang, G., Zhang, S., Yao, J., Keita, B., Nadjo, L., Zhi, L., 2012. Small 8 (9), 1398–1406.
Liu, R., Yu, X., Zhang, G., Zhang, S., Cao, H., Dolbecq, A., Mialane, P., Keita, B., Zhi, L., 2013. J. Mater. Chem. A 1 (38), 11961–11969.
Lu, X., Wang, X., Jin, J., Zhang, Q., Chen, J., 2014. Biosens. Bioelectron. 62 (0), 134–139.
Nishimoto, Y., Yokogawa, D., Yoshikawa, H., Awaga, K., Irle, S., 2014. J. Am. Chem. Soc. 136 (25), 9042–9052.
Palanisamy, S., Chen, S.M., Sarawathi, R., 2012. Sens. Actuators B 166–167 (0), 372–377.
Park, J.-B., Lee, J., Yoon, C.S., Sun, Y.-K., 2013. ACS Appl. Mater. Interfaces 5 (24), 13426–13431.
Rhule, J.T., Hill, C.L., Judd, D.A., Schinazi, R.F., 1998. Chem. Rev. 98 (1), 327–357.
Roy-Mayhew, J.D., Aksay, I.A., 2014. Chem. Rev. 114 (12), 6323–6348.
Ryoo, R., Joo, S.H., Jun, S., 1999. J. Phys. Chem. B 103 (37), 7743–7746.
Saleh Ahammad, A.J., Lee, J.J., Rahman, M.A., 2009. Sensors 9 (4), 2289–2319.
Scherbahn, V., Putze, M.T., Dietzel, B., Heinlein, T., Schneider, J.J., Lisdat, F., 2014. Biosens. Bioelectron. 61 (0), 631–638.
Stracke, J.J., Finke, R.G., 2014. ACS Catal. 4 (3), 909–933.
Teymourian, H., Salimi, A., Hallaj, R., 2012. Biosens. Bioelectron. 33 (1), 60–68.
Vu, A., Li, X., Phillips, J., Han, A., Smyrl, W.H., Bühlmann, P., Stein, A., 2013. Chem. Mater. 25 (21), 4137–4148.
Wang, K., Wang, Y., Liang, Z., Liang, Y., Wu, D., Song, S., Tsiakaras, P., 2014. Appl. Catal. B: Environ. 147, 518–525.
Wang, S.-F., Xie, F., Hu, R.-F., 2007. Sens. Actuators B: Chem. 123 (1), 495–500.
Wang, Y., Neyman, A., Arkhangelsky, E., Gitis, V., Meshi, L., Weinstock, I.A., 2009. J. Am. Chem. Soc. 131 (47), 17412–17422.
Wu, Z., Wu, W.D., Liu, W., Selomulya, C., Chen, X.D., Zhao, D., 2013. Angew. Chem. Int. Ed. 52 (51), 13764–13768.
Xing, X., Liu, R., Wang, Z., Ren, B., Jiang, Z., Zhao, H., Cao, H., Zhang, G., Zhang, T., 2013a. J. Nanosci. Nanotechnol. 13 (7), 4616–4621.
Xing, X., Liu, R., Yu, X., Zhang, G., Cao, H., Yao, J., Ren, B., Jiang, Z., Zhao, H., 2013b. J. Mater. Chem. A 1 (4), 1488–1494.
Zhang, G., Keita, B., Biboum, R.N., Miserque, F., Berthet, P., Dolbecq, A., Mialane, P., Catala, L., Nadjo, L., 2009. J. Mater. Chem. 19 (45), 8639–8644.
Zhang, M., Weinstock, I.A., Wang, Y., 2014a. J. Clust. Sci. 25 (3), 771–779.
Zhang, Y., Bo, X., Luhana, C., Guo, L., 2011. Electrochim. Acta 56 (17), 5849–5854.
Zhang, Y., Bo, X., Nsabimana, A., Luhana, C., Wang, G., Wang, H., Li, M., Guo, L., 2014b. Biosens. Bioelectron. 53 (0), 250–256.
Zhi, J., Zhao, W., Liu, X., Chen, A., Liu, Z., Huang, F., 2014. Adv. Funct. Mater. 24 (14), 2013–2019.